Enhancement of Photovoltaic Response in Multilayer MoS_2 Induced by Plasma Doping

Sungjin Wi,[†] Hyunsoo Kim,[‡] Mikai Chen,[†] Hongsuk Nam,[†] L. Jay Guo,[‡] Edgar Meyhofer,[†] and Xiaogan Liang[†,*]

[†]Department of Mechanical Engineering and [‡]Department of Electrical Engineering and Computer Science, University of Michigan, Ann Arbor, Michigan 48109, United States

ABSTRACT Layered transition-metal dichalcogenides hold promise for making ultrathin-film photovoltaic devices with a combination of excellent photovoltaic performance, superior flexibility, long lifetime, and low manufacturing cost. Engineering the proper band structures of such layered materials is essential to realize such potential. Here, we present a plasma-assisted doping approach for significantly improving the photovoltaic response in multilayer MoS_2. In this work, we fabricated and characterized photovoltaic devices with a vertically stacked indium tin oxide electrode/multilayer MoS_2/metal electrode structure. Utilizing a plasma-induced p-doping approach, we are able to form p−n junctions in MoS_2 layers that facilitate the collection of photogenerated carriers, enhance the photovoltages, and decrease reverse dark currents. Using plasma-assisted doping processes, we have demonstrated MoS_2-based photovoltaic devices exhibiting very high short-circuit photocurrent density values up to 20.9 mA/cm^2 and reasonably good power-conversion efficiencies up to 2.8% under AM1.5G illumination, as well as high external quantum efficiencies. We believe that this work provides important scientific insights for leveraging the optoelectronic properties of emerging atomically layered two-dimensional materials for photovoltaic and other optoelectronic applications.

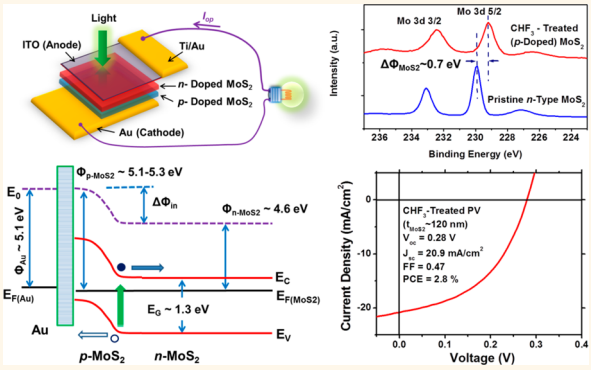

KEYWORDS: 2D materials · MoS_2 · photovoltaics · doping · nanofabrication · p−n junction

Two-dimensional (2D) layered transition metal dichalcogenides (LTMDs) have gained significant interest because of their desirable electronic, photonic, and mechanical properties, versatile chemistry, and large natural abundance.[1−5] In particular, the semiconducting LTMDs (*e.g.*, WSe_2, WS_2, and MoS_2) exhibit attractive optoelectronic properties, *e.g.*, the unique valley-polarized optical response observed in MoS_2, fast photoresponse speed, and very high light absorption over a broad range of wavelengths.[6,7] In particular, a single semiconducting LTMD layer (~0.5 nm thick) can absorb as much sunlight as 50 nm of Si (or 12 nm of GaAs) and generate photocurrents as high as 4.5 mA/cm^2.[8] This high light absorption is attributed to the rich van Hove singularity peaks in the electronic density of states (DOS) of these semiconducting LTMDs (including monolayer, few-layer, and multilayer LTMDs), which results in a sharp rise of joint density of states (JDOS) in the visible light range and ensures relatively strong light-matter interactions.[8−10] Therefore, semiconducting LTMDs can potentially be used for making flexible ultrathin photovoltaic (PV) cells with 1−3 orders of magnitude higher power densities (*i.e.*, solar power converted per unit volume of photoactive materials) than the best existing thin-film PV cells.[8,9,11] It should be noted that although power density is not a standard figure of merit for PV performance, the higher power density could decrease the needed photoactive layer thickness for achieving a given amount of light absorption and, therefore, enable highly flexible PV cells with substantial power-conversion efficiency (PCE) and external quantum efficiency (EQE) as well as thin-film photodetectors with sizable responsivity.

* Address correspondence to xiaoganl@umich.edu.

Received for review March 7, 2014 and accepted May 1, 2014.

Published online May 01, 2014
10.1021/nn5013429

Semiconducting LTMDs are anticipated to offer additional advantages in serving as PV active materials, including (i) excellent chemical stability (*i.e.*, LTMDs are chemically stable 2D crystals),[5] (ii) good mechanical flexibility and durability comparable to graphene,[12] and (iii) superior electronic and electrical properties for fabricating functional interfaces with other 2D materials (*e.g.*, graphene-based conductors and boron nitride (BN)-based dielectrics) because they can form high-quality heterojunction and interfaces with an extremely low areal density of dangling bonds and charge traps.[13,14] Such heterojunctions could address the challenges associated with interfacial recombination centers that impact the photovoltaic efficiencies. It should be noted that such stacked 2D heterostructures are distinct from the stacked thin films of 3D materials that usually have a high density of interfacial traps. A last advantage is (iv) low production cost; *i.e.*, LTMD-based ultrathin PV cells, similar to graphene-based devices, could potentially be manufactured on low-cost flexible substrates by using roll-to-roll deposition and printing processes.[15−17]

Although semiconducting LTMDs exhibit very strong light-matter interactions and very high light absorption coefficients,[4,8−10] LTMD-based PV cells with superior PV performance have not been demonstrated. In particular, the current single and few-layer LTMD PV and photodetector devices only showed a high photocurrent density per unit photoactive layer thickness (*e.g.*, 4.5 mA/cm^2 per LTMD monolayer).[4,8−10] To obtain sizable photocurrents and photovoltage outputs for practical PV applications, multilayer LTMD PV devices are needed. However, the current multilayer LTMD PVs exhibit relatively poor values of critical figures of merit, including low short-circuit photocurrent density (J_{sc} < 6 mA/cm^2), external quantum efficiency (EQE < 40% over the visible light range), open-circuit voltage (V_{oc} < 0.6 V), fill factor (FF < 0.55), and photoconversion efficiency (PCE < 2%).[8,9,18,19] To improve these performance parameters, we (or the researchers in this field) need to advance the knowledge and technology for tailoring the band structures of LTMD PV devices. In particular, new approaches are needed for creating built-in potentials (or electric fields) inside LTMD photoactive layers that can facilitate the collection of photogenerated carriers, enhance the output photovoltages, and effectively suppress the reverse dark saturation currents. Toward this goal, several recently published works have provided important insights.[8,14,18,19] For example, Britnell *et al*. studied the photocurrent generated in WS_2/graphene stacks and found that the doping at graphene contacts induced by gating or moisture can induce a built-in potential inside WS_2 photoactive layers that can separate photogenerated electron−hole (e−h) pairs and generate photocurrents at zero bias.[8] Shanmugam *et al*. fabricated Schottky-barrier solar cells based on multilayer MoS_2, in which the built-in potential at the Schottky junction separates the e−h pairs.[18] Fontana *et al*. demonstrated gated MoS_2 Schottky junction devices with Pd/Au electrode pairs that exhibit an asymmetric, diode-like photoresponse behavior.[19] Yu *et al*. realized the modulation of photocurrents and EQEs in vertically stacked graphene−MoS_2 heterostructures by using the gating electric field penetrating through the graphene electrodes with a weak screening effect.[14] More recently, Ross *et al*., Baugher *et al*., and Pospischi *et al*. (three different teams) created electrically tunable excitonic light-emitting diodes (LEDs), photodiodes, and PV devices, in which dual-gate structures are used for electrostatically doping monolayer WSe_2 channels and hence forming lateral WSe_2-based p−n junctions.[20−22] Such p−n junctions result in bright electroluminescence at the room temperature,[20] peak EQE ~0.2% at λ = 522 nm for monolayers,[21] and sizable power-conversion efficiency of ~0.5% for lateral monolayer semitransparent PV devices.[22] These lateral photodiode devices based on WSe_2 monolayers, in comparison with those based on MoS_2 monolayers, exhibit comparable EQE values in the photovoltaic mode but the higher electroluminescence efficiencies.[20−22] However, the implementation of dual-gate structures cannot enable the permanent doping effects in LTMD photoactive layers and is not convenient for practical optoelectronic applications.

In this paper, we report that plasma-assisted doping can serve as a new and very effective method to generate p−n junction type MoS_2 PV devices with the built-in potentials to separate the photogenerated charges, resulting in significantly improved PV response performance. We have fabricated PV devices consisting of a vertically stacked indium tin oxide (ITO)/pristine MoS_2/plasma-doped MoS_2/Au structure, which exhibit reasonably good PCE values up to 2.8% and superb J_{sc} values up to 20.9 mA/cm^2 under AM1.5G illumination, as well as high EQE values in the range of 37−78% for wavelengths between 300 and 700 nm. This work provides important scientific insights for leveraging unique optoelectronic properties of LTMDs for photovoltaic and other optoelectronic applications.

RESULTS AND DISCUSSION

Figure 1 illustrates the steps for fabricating PV devices with MoS_2 photoactive layers. First, a pristine MoS_2 ingot stamp bearing protrusive mesa features is fabricated by using a lithography method previously published (Figure 1 (a)).[17] Such mesa features define the patterns of to-be-exfoliated multilayer MoS_2 flakes that will serve as PV photoactive layers. Before the exfoliation, the top surface of the stamp is treated with a plasma species (*e.g.*, O_2, SF_6, or CHF_3) to induce doping in the top MoS_2 layers (Figure 1 (b)) according to the previous report.[23] Following this treatment, the

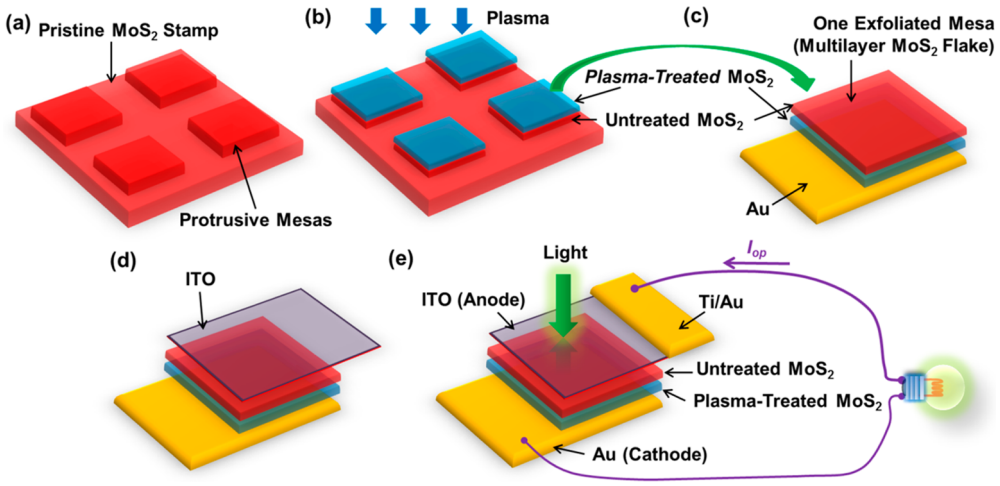

Figure 1. Flowchart for fabricating PV devices with plasma-treated MoS_2 photoactive layers: (a) preparation of an untreated (pristine) MoS_2 ingot stamp; (b) plasma-assisted treatment of the top surface layers of the MoS_2 stamp; (c) mechanical exfoliation printing of protrusive mesas (*i.e.*, multilayer MoS_2 flakes) with plasma-treated surfaces in contact with the underlying Au electrodes; (d) fabrication of ITO electrodes in contact with the untreated surfaces of the MoS_2 flakes; (e) photovoltaic characterization using a standard AM1.5G solar simulator.

protrusive mesa features are mechanically exfoliated onto 50-nm-thick Au electrodes that have been prefabricated on a glass substrate by using photolithography followed with metalization and lift-off (Figure 1 (c)).[17] The resulting multilayer MoS_2 flakes range in thickness from 10−140 nm. A second electrode of indium tin oxide (ITO) is fabricated on the untreated pristine surfaces of MoS_2 flake pestals (Figure 1 (d)). Finally, a standard AM1.5G solar simulator is used for the PV characterization (Figure 1 (e)). Other fabrication and characterization details are described in the Method and Material.

Figure 2 (a) displays an optical micrograph (OM) of an exemplary MoS_2 ingot stamp bearing 20 μm size mesa structures that was treated with CHF_3 plasma. Figure 2 (b) shows an image of MoS_2 flakes mechanically exfoliated onto a SiO_2/Si substrate (oxide thickness, 300 nm) with different thicknesses that are corresponding to different flake colors. Most exfoliated flakes are 20−150 nm thick, as measured by using an atomic force microscope (AFM). Though not suitable for immediate scale-up PV applications, this exfoliation printing method provides useful MoS_2 sample arrays for systematically studying the effect of a MoS_2 photoactive layer thicknesses on PV performance parameters. Figure 2 (c) displays the top-view image of a vertically stacked Au/plasma-treated MoS_2/untreated MoS_2/ITO structure. It should be noted that there is a marginal MoS_2 area that is not fully sandwiched by ITO and Au electrodes. To study the PV effect associated with carriers moving along the vertical direction, this marginal MoS_2 area is etched away by using a SF_6 plasma recipe. Figure 2 (d) shows the image of the device structure after the SF_6 plasma etching. The final area of the MoS_2 flake is defined as the photoactive area for evaluating J_{sc} and EQE values, as indicated by

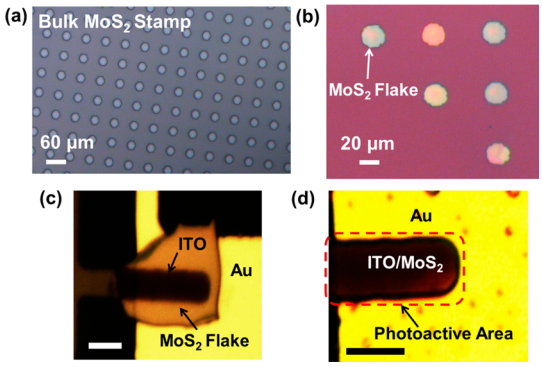

Figure 2. Optical micrographs of (a) the surface of a MoS_2 ingot stamp that has been patterned with 20 μm diameter, 200 nm high mesa features and subsequently blank-treated by using a CHF_3-based plasma protocol; (b) MoS_2 flakes that were mechanically exfoliated onto a SiO_2/Si substrate (oxide thickness, 300 nm); (c) a PV device with a vertically stacked ITO/pristine MoS_2/CHF_3 plasma-treated MoS_2/Au structure before the final SF_6 etching (the scale bar is 10 μm); (d) the final PV device (the scale bar is 10 μm). In the final device, the marginal MoS_2 area that is not covered by ITO has been completely removed by SF_6 plasma etching. The dashed box denotes the photoactive area (*i.e.*, the final MoS_2 flake area) that is used for evaluating J_{sc} and EQE values.

the dashed box in Figure 2 (d). Here, it is noted that the MoS_2 photoactive area sandwiched by Au and ITO electrodes appears to be very dark under the OM illumination. This implies a high light absorption in MoS_2 layers, which is an important basis for achieving high J_{sc} and EQE values in MoS_2 PV devices.

For a systematic study, first we fabricated several MoS_2 PV devices treated with different plasma species (*i.e.*, O_2, SF_6, CF_4, and CHF_3) and performed a brief $I-V$ characterization under illumination of 532 nm laser light (power density, P_{laser} = 283 mW/cm^2). The plasma treatment protocols are described in details in the

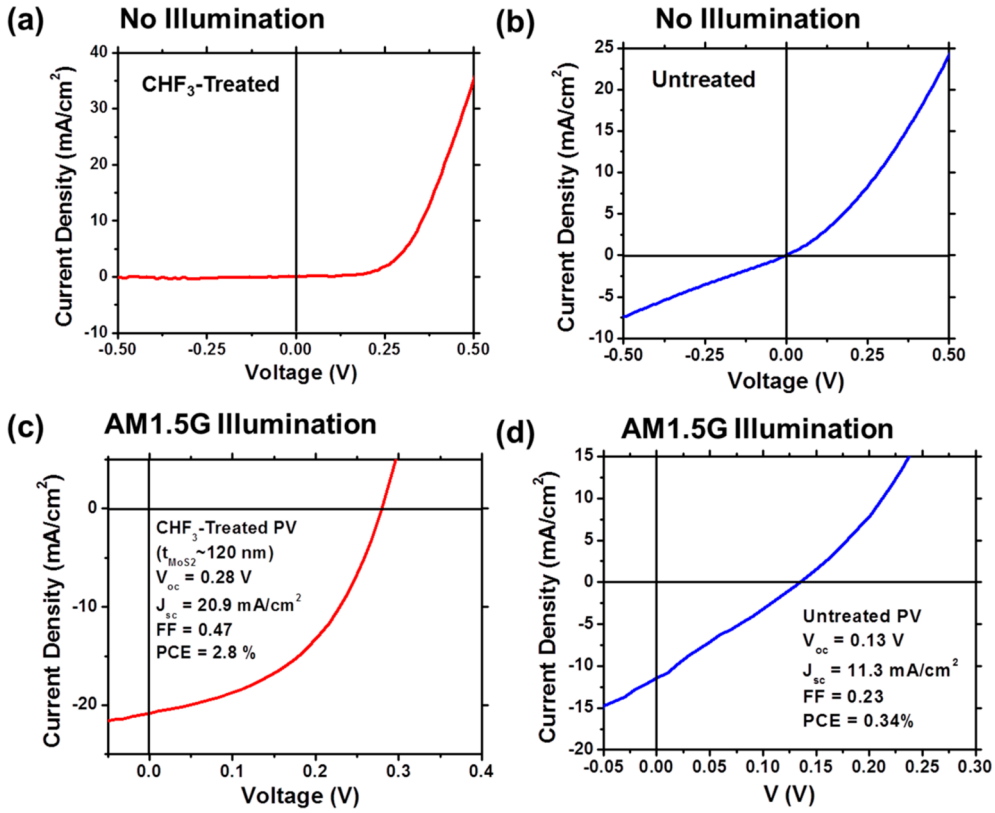

Figure 3. One example of the comparison between plasma-treated and untreated MoS_2 PV devices: (a, b) Current density−voltage ($J-V$) characteristics of a CHF_3 plasma-treated PV device and an untreated control device, respectively, which were measured with no illumination. Both devices have the same MoS_2 photoactive layer thickness of ~120 nm. (c, d) $J-V$ characteristics, measured under illumination of AM1.5G simulated sunlight (power density, 100 mW/cm^2), of these two PV devices, respectively. The plasma-treated PV device exhibits the higher rectification degree (*i.e.*, $I_F/I_R > 10^4$ at $|V| = 0.5$ V) and PV performance parameters (*i.e.*, $V_{oc} = 0.28$ V, $J_{sc} = 20.9$ mA/cm^2, FF = 0.47, and PCE = 2.8%) in comparison with those of the untreated PV device (*i.e.*, $I_F/I_R \sim 3$ at $|V| = 0.5$ V, $V_{oc} = 0.13$ V, $J_{sc} = 11.3$ mA/cm^2, FF = 0.23, PCE = 0.34%).

Method and Material. Figure S1 in the Supporting Information displays the current density−voltage ($J-V$) characteristic curves of the MoS_2 PV devices treated with O_2, SF_6, CF_4, and CHF_3 plasmas. For all devices, the MoS_2 photoactive layer thickness is ~100 nm. This brief characterization shows that the CHF_3 plasma-treated PV devices exhibit the highest PV performance in terms of the highest values of J_{sc}, V_{oc}, FF, and PCE parameters. Here, PCE = $J_{sc}V_{oc}FF/P_{laser}$. Therefore, our following analysis and discussion focus on CHF_3 plasma-treated MoS_2 PV devices.

Figures 3 (a) and (b) show the $J-V$ characteristics, measured without illumination, of a CHF_3 plasma-treated PV device and an untreated control device. Both devices have the same MoS_2 layer thickness of 120 nm. In comparison with the untreated device, the plasma-treated PV device exhibits a much more prominent diode-like behavior with a high degree of current rectification (forward/reverse current ratio, $I_F/I_R > 10^4$ at $|V| = 0.5$ V), very small reverse dark current (on the order of 1 μA/cm^2), and relatively high shunt resistance of ~790 Ω cm^2. The untreated control device exhibits a quite weak degree of rectification ($I_F/I_R \sim 3$ at $|V| = 0.5$ V), which is attributed to the shallow Schottky barrier formed at the pristine MoS_2/Au interface. Parts (c) and (d) of Figure 3 show the $J-V$ characteristics of these two devices measured under illumination of AM1.5G simulated sunlight (power density, P_{sun} = 100 mW/cm^2). The untreated PV device exhibits a reasonably high J_{sc} value of 11.3 mA/cm^2 that is attributed to the high light absorption coefficient of MoS_2 but relatively poor values of V_{oc} (0.13 V), FF (0.23), and PCE (0.34%). Here, PCE = $J_{sc}V_{sc}FF/P_{sun}$. In contrast, the plasma-treated PV device exhibits a significantly improved PV response with (or as evidenced by) J_{sc} = 20.9 mA/cm^2, V_{oc} = 0.28 V, FF = 0.47, and PCE = 2.8%. Inparticular, this J_{sc} value is comparable with the J_{sc} data of some superb thin-film solar cells based on single-crystal semiconductors.[24,25] For this specific example, the CHF_3 plasma treatment process results in approximately 2-fold increase in J_{sc}, 2-fold increase in V_{oc}, 2-fold increase in FF, and about 8-fold increase in PCE.

To verify the high J_{sc} values observed in our MoS_2 PV devices, we measured the EQE spectra of these two PV devices for wavelengths (λ) ranging from 300 to 800 nm using a luminescence spectrometer (Figure 4 (a)) (note that the EQE measurements are independent from the PV characterizations under AM1.5G illumination to check the measurement consistency). In this

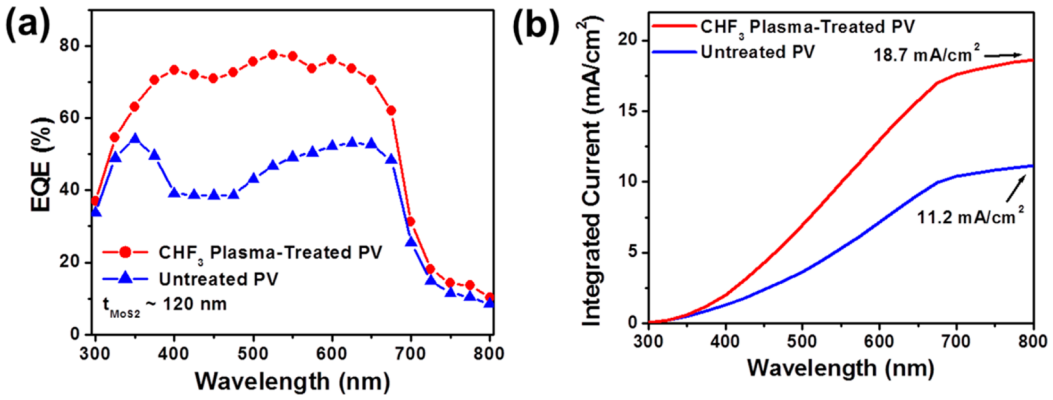

Figure 4. EQE measurements for further confirming the high J_{sc} values measured using an AM1.5G solar simulator: (a) EQE spectra, measured at wavelengths λ = 300−800 nm, of a CHF_3 plasma-treated PV device (red circles) and an untreated PV device (blue triangles). Both devices have the same MoS_2 layer thickness of 120 nm. (b) Integral of the overlap between the measured EQE data and the standard AM1.5G spectrum over a wavelength range of 300 to 800 nm, which yields calculated J_{sc} values of 18.7 mA/cm^2 and 11.2 mA/cm^2 for the plasma-treated PV device and the untreated control device, respectively.

measurement, the EQE at a wavelength λ is extracted from the J_{sc} value measured under the illumination at λ with incident power density P_λ (*i.e.*, EQE (λ) = (J_{sc}/P_λ)($hc/e\lambda$), where h, c, and e are Planck's constant, the speed of light, and the electron charge, respectively). The EQE values of the untreated PV device are in the range of 34−54% for λ = 300−700 nm, which are comparable with previously reported EQE data of undoped MoS_2 photoactive layers.[8,18] In comparison to the untreated device, the CHF_3 plasma-treated device exhibits significantly enhanced EQE values at all wavelengths between 300 and 700 nm, which are in the range of 37−78%. Figure 4 (b) plots the integral of the overlap between these measured EQE values and the standard AM1.5G spectrum over a wavelength range of 300−800 nm, which yields calculated J_{sc} values of 18.7 and 11.2 mA/cm^2 for the plasma-treated PV device and the untreated control device, respectively. Such J_{sc} values calculated from EQE data are consistent with the J_{sc} values independently measured using the AM1.5G solar simulator. The remaining small discrepancy between these two groups of J_{sc} values is attributed to the uncounted photocurrent density contributions from other wavelengths that are not covered in our EQE measurements and the EQE-based calculation of J_{sc} values.

To demonstrate the repeatability for achieving high J_{sc} values in plasma-treated PV devices with MoS_2 photoactive layer thicknesses close to that of the device shown in Figure 3 (c), Figure S2 (a)−(d) in the Supporting Information lists the J−V characteristics of another four CHF_3 plasma-treated PV devices that were fabricated in the same batch as the one discussed above. The MoS_2 photoactive layer thicknesses of these devices range from 81 to 120 nm. All of them exhibit very high J_{sc} values (18.0−21.7 mA/cm^2) and reasonably good PCEs (1.7−2.56%) under AM1.5G illumination, as well as a good consistency between the J_{sc} values measured by the solar simulator and the calculated J_{sc} values based on EQE data (parts (e) and (f) of Figure S2 (Supporting Information) show one of examples of such consistency for these PV devices).

Figure 4 (a) and Figure S2 (e) (Supporting Information) also demonstrate that the EQE values of both untreated and plasma-treated MoS_2 PV devices remain relatively high, even at wavelengths as short as 300 nm (~34% for the untreated device; 37−48% for the plasma-treated ones). Most PV devices based on conventional semiconductors (*e.g.*, Si and III−V compounds) typically exhibit significantly depressed EQE values for λ < 400 nm, which is attributed to the blue-response-reduction effect associated with the front surface recombination of photogenerated e−h pairs.[26−29] Here, our EQE results show that our MoS_2 PV devices exhibit a mitigated reduction of the blue response, which could be attributed to the low density of recombination centers on the front surfaces of 2D MoS_2 layers (*i.e.*, the surfaces not treated by plasmas). Although such a relatively high blue response is not greatly beneficial for the solar cell applications under AM1.5G condition (the AM1.5G spectrum is significantly cut off at λ < 280 nm), it is beneficial for making new blue and ultraviolet (UV) photodetectors. Based on the EQE spectrum of a CHF_3 plasma-treated PV device shown in Figure S2 (e) (Supporting Information), we extracted the photovoltaic-mode (*i.e.*, zero-bias mode) responsivity spectrum $R(\lambda)$ = EQE × ($e\lambda/hc$) for this device, as shown in Figure S3 (a) (Supporting Information). Even under zero bias, this device still exhibits a high responsivity >90 mA/W for λ = 300−700 nm. Figure S3 (b) (Supporting Information) displays its I−V characteristic curves measured under dark (blue curve) and illumination (532 nm laser light with excitation power of 283 mW/cm^2) (green curve) conditions. This device exhibits high light to dark current ratios (10^2 to 10^4) at zero and reverse biases.

To further verify the role of plasma treatment in the photovoltaic response enhancement and also identify the effect of MoS_2 thickness on PV performance

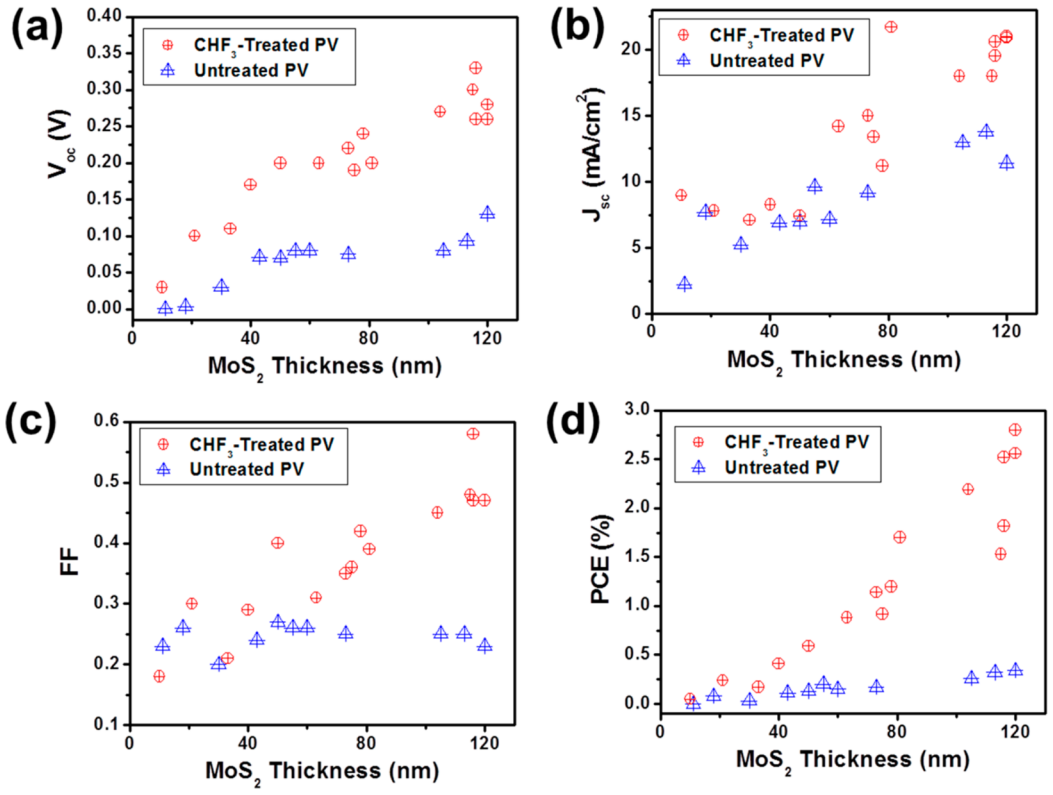

Figure 5. Additional data systematically showing the comparison between plasma-treated and untreated MoS_2 PV devices in photovoltaic response performance: V_{oc} (a), J_{sc} (b), FF (c), and PCE (d) data of multiple CHF_3 plasma-treated (denoted by red circles) and untreated (denoted by blue triangles) MoS_2-based PV devices, which are plotted as the functions of MoS_2 thickness. In any range of the MoS_2 thickness, plasma-treated devices exhibit statistically higher values of V_{oc}, FF, J_{sc}, and PCE parameters in comparison with untreated ones.

parameters, we fabricated a set of CHF_3 plasma-treated and untreated PV devices with a broad range of MoS_2 layer thickness (10−120 nm). Figure S4 in the Supporting Information lists the $J-V$ characteristics, measured under AM1.5G illumination, of all of these devices. Figure 5 displays (a) V_{oc}, (b) J_{sc}, (c) FF, and (d) PCE data of all PV devices (red circles are for CHF_3 plasma-treated devices; blue triangles are for untreated devices), which are plotted as the functions of MoS_2 layer thicknesses. Figure 5 clearly shows that plasma-treated PV devices exhibit higher values of V_{oc}, J_{sc}, FF, and PCE as compared to untreated devices of similar MoS_2 thickness. For MoS_2 thicknesses above 60 nm, the plasma treatment process induces the more prominent photovoltaic response enhancement. While our current fabrication processes lead to observable device-to-device variation in PV parameters, including the variation among devices of similar MoS_2 thickness, the statistical properties of the PV data shown in Figure 5 are highly consistent with our view that the plasma treatment significantly improves the photovoltaic response of MoS_2-based PV devices.

Figure 5 also shows that the PV parameters of CHF_3 plasma-treated devices increase with increasing the MoS_2 layer thickness in the range of 10−120 nm. Devices with MoS_2 thicknesses of 80−120 nm exhibit the highest PV response performance (*i.e.*, V_{oc}: 0.2−0.33 V, J_{sc}: 18−21.7 mA/cm^2, FF: 0.42−0.58, PCE: 1.7−2.8%). Our current transfer-printing process is not effective in producing MoS_2 flakes thicker than 130 nm.[17] However, using the mechanical exfoliation method previously reported,[1] we fabricated six CHF_3 plasma-treated PV devices with MoS_2 thicknesses in the range of 210 to 500 nm (Figure S5 in the Supporting Information displays the $J-V$ characteristics of these devices under AM1.5G illumination). These thicker MoS_2 PV devices exhibit prominent diode-like $J-V$ characteristics, but they show a very weak PV response (*i.e.*, V_{oc}: 0.1−0.15 V, J_{sc}: 0.62−4.92 mA/cm^2, FF: 0.21−0.33, PCE: 0.018 to 0.25%). These results indicate that the performance of plasma-treated MoS_2 PV devices highly depends on MoS_2 layer thickness, and that the optimal MoS_2 thickness, which could result in the highest PCE, should be in the range of 120−210 nm. Future efforts will seek to develop new nanomanufacturing approaches that can result in a high yield of MoS_2 flakes or large films with thickness values in this range.

To understand the physical mechanism responsible for the plasma treatment-induced enhancement of current rectification and photovoltaic responses observed in MoS_2 PV devices, we measured X-ray photoelectron spectra (XPS) of plasma-treated and untreated MoS_2 surfaces. Figure 6 (a) shows the Mo $3d_{5/2}$ and Mo $3d_{3/2}$ XPS peaks of CHF_3 plasma-treated and untreated

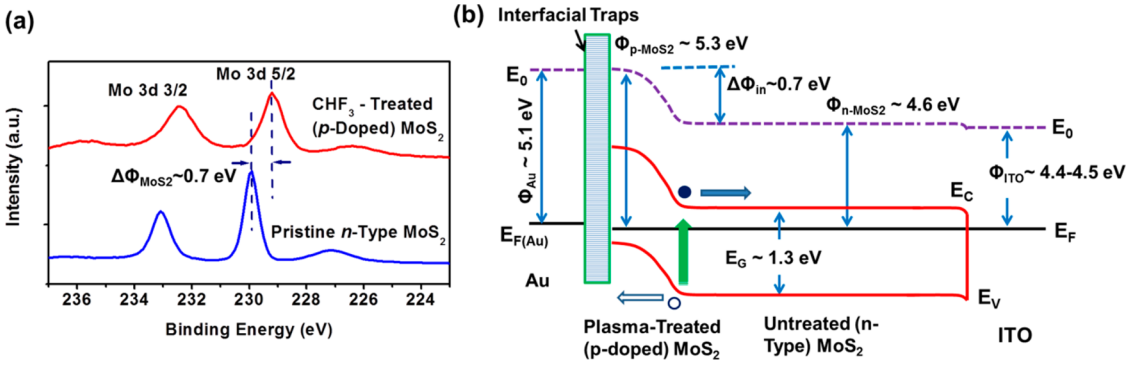

Figure 6. XPS surface analysis of plasma-treated MoS_2 surfaces for understanding the band structure of plasma-doped MoS_2 PV devices: (a) Mo $3d_{5/2}$ and Mo $3d_{3/2}$ XPS peaks of CHF_3 plasma-treated and untreated (pristine) MoS_2 surfaces, which show that the plasma treatment results in a negative shift of the elemental electron binding energy and therefore the p-doping characteristics in treated MoS_2 layers. (b) Schematic band diagram of a CHF_3 plasma-treated MoS_2 PV device with vertically stacked Au/plasma-treated (or p-doped) MoS_2/untreated (or n-type) MoS_2/ITO regions, which has a p−n junction with built-in potential $\Delta\Phi_{in} = \Phi_{p\text{-}MoS2} - \Phi_{n\text{-}MoS2} \sim 0.7$ eV.

(pristine) MoS_2 surfaces. In comparison with the Mo $3d_{5/2}$ and Mo $3d_{3/2}$ peaks of the untreated MoS_2 surface, the relevant peaks of the CHF_3 plasma-treated surface are wider, and their maxima shift toward the lower binding energy values. The relative shift ($\Delta\Phi_{MoS2}$) is measured to be about 0.7 eV. Such a downshift of XPS peaks can serve as an indicator of the p-doping in MoS_2, because it is corresponding to a relative shift of the Fermi level toward the valence band edge.[30−32] This XPS characterization also strongly suggests that a p−n junction (*i.e.*, a built-in potential ($\Delta\Phi_{in}$)) could be formed in a MoS_2 flake with one surface treated with plasma. The CHF_3 plasma-induced p−n junction is estimated to have a built-in potential $\Delta\Phi_{in} \sim \Delta\Phi_{MoS2} \sim 0.7$ eV. Additional in-depth analysis and discussion about physical mechanisms involved in plasma doping processes (*e.g.*, the physical mechanism responsible for plasma-induced p-doping, the depth profiling of dopants, as well as the spatial uniformity of p−n junction built-in potentials) are discussed in the Supporting Information.

Based on the XPS results, we plot the band diagram of our MoS_2 PV devices with vertically stacked ITO/untreated n-type MoS_2/CHF_3 plasma-treated p-type MoS_2/Au regions, as illustrated in Figure 6 (b). The interface between plasma-doped and undoped MoS_2 regions is expected to be a p−n junction with a built-in potential $\Delta\Phi_{in} \sim 0.7$ eV, as implied by the XPS data. The electric field associated with this built-in potential barrier could effectively facilitate the separation and collection of photogenerated e−h pairs, therefore resulting in the higher J_{sc} and EQE values for plasma-doped MoS_2 PV devices as compared to those for undoped ones. This built-in potential barrier is also responsible for the increased open-circuit voltage (V_{oc}). In addition, the plasma doping-induced p−n junctions can result in a strong diode-like transport characteristic in MoS_2 PV devices, which feature a high degree of current rectification. Such a rectifying diode behavior effectively suppresses the reverse dark current and increases the shunt resistance of a MoS_2 PV diode, resulting in the enhancement of the fill factor (FF).

Although the plasma-induced enhancement of photovoltaic response in MoS_2 PV devices could be attributed to the formation of p−n junctions in MoS_2 photoactive layers, the effect of the Schottky junction barriers potentially formed at ITO/MoS_2 and Au/MoS_2 interfaces needs to be further analyzed and justified. The interface between ITO and untreated n-type MoS_2 is expected to be a quasi-Ohmic contact, because the work function of untreated MoS_2 ($\Phi_{n\text{-}MoS2} \sim 4.6$ eV) is very close to that of ITO ($\Phi_{ITO} \sim 4.4-4.5$ eV).[33] Therefore, only a negligible Schottky barrier built-in potential would be formed at ITO/untreated MoS_2 interfaces. To experimentally verify this band alignment analysis, we fabricated lateral ITO/untreated MoS_2/ITO structures and measured their *I*−*V* characteristics. Parts (a) and (b) of Figure S8 (Supporting Information) show the OM image and the *I*−*V* characteristic curve of a representative device, respectively. The highly linear and symmetric *I*−*V* curve indicates that there is a very shallow Schottky junction barrier formed at ITO/untreated MoS_2 interfaces. Figure S9 (a) (Supporting Information) illustrates the ideal band diagram of an Au/untreated pristine MoS_2 interface, which is plotted without taking into account the Fermi level pinning effect due to the interfacial traps. Here, the band alignment is completely determined by the work functions of pristine MoS_2 ($\Phi_{n\text{-}MoS2} \sim 4.6$ eV) and Au ($\Phi_{Au} \sim 5.1$ eV).[18] The built-in potential ($\Delta\Phi_{in}$) of the Schottky barrier at such an Au/untreated MoS_2 interface is ideally estimated to be $\Delta\Phi_{in} = \Phi_{Au} - \Phi_{n\text{-}MoS2} \sim 0.5$ eV. Shanmugam *et al.* attributed the photovoltaic response observed in their MoS_2 PV devices to such a Schottky barrier effect.[18] The photovoltaic response observed in our undoped PV devices could also be attributed to it. However, the substantially poorer PV performance of our undoped PV devices in comparison with our plasma-doped ones

suggests that the real Schottky barrier height in our undoped PV devices may be significantly smaller than 0.5 eV (*i.e.*, $\Phi_{Au} - \Phi_{n\text{-}MoS2}$), which could be attributed to the Fermi level pinning effect induced by the interfacial traps at Au/pristine MoS_2 interfaces. Figure S9 (b) (Supporting Information) qualitatively illustrates the band diagram of an Au/untreated MoS_2 interface that is plotted with taking into account the Fermi level pinning effect that could result in $\Delta\Phi_{in} < \Phi_{Au} - \Phi_{n\text{-}MoS2}$. We also postulate that the real Au/MoS_2 Schottky barrier heights may highly depend on the specific conditions for producing and processing MoS_2 flakes.

Based on the XPS result, the work function of CHF_3 plasma-treated (or p-doped) MoS_2 layers is estimated to be $\Phi_{p\text{-}MoS2} \sim 5.3$ eV that is close to the work function of Au (*i.e.*, $\Phi_{Au} \sim 5.1$ eV). Therefore, an Au/p-doped MoS_2 interface would be likely a quasi-Ohmic contact with a very shallow Schottky barrier, as illustrated in the band diagram in Figure S10 (a) (Supporting Information) that is plotted without taking into account the Fermi level pinning effect. However, the band alignment at such Au/p-doped MoS_2 interfaces could be complicatedly affected by the interfacial traps, as illustrated in Figure 6 (b). To experimentally evaluate the transport property of such Au/p-doped MoS_2 interfaces, we fabricated a back-gated MoS_2 field-effect transistor (FET) using the method previously reported.[17,23] The top surface of the MoS_2 channel was blank-treated with CHF_3 plasma to form a pair of Au/p-doped MoS_2 drain/source contacts. Figure S10 (b) in the Supporting Information illustrates the cross-sectional view of the FET structure labeled with critical dimensions. Figure S10 (c) (Supporting Information) shows the output characteristics (*i.e.*, drain-source current (I_{DS}) versus drain-source voltage (V_{DS}) curves measured under different gate voltages (V_G)) of the FET. This FET exhibits highly linear and symmetric $I_{DS} - V_{DS}$ characteristics under all gate voltages, which implies that the Au/p-doped MoS_2 interfaces are quasi-Ohmic contacts with a very shallow Schottky barrier. This analysis further supports our view that it is the p−n junctions formed in MoS_2 photoactive layers that give rise to the high photovoltaic response observed in plasma-treated MoS_2 PV devices.

It is known that in layered semiconductors, the interlayer transport characteristic parameters (*e.g.*, mobility and saturation velocity) are worse than the corresponding parameters for the in-plane transport case. To evaluate the interlayer transport properties in multilayer MoS_2, we further studied the diode transport characteristics of our PV devices in different bias regimes. Figure 7 shows the forward bias $J-V$ characteristic curve, measured without illumination, of a PV diode consisting of vertically stacked Au/p-doped MoS_2/n-type MoS_2/ITO layers. The total MoS_2 thickness (or the channel length of this vertical diode) is $L \sim 120$ nm. This vertical MoS_2 diode exhibits different

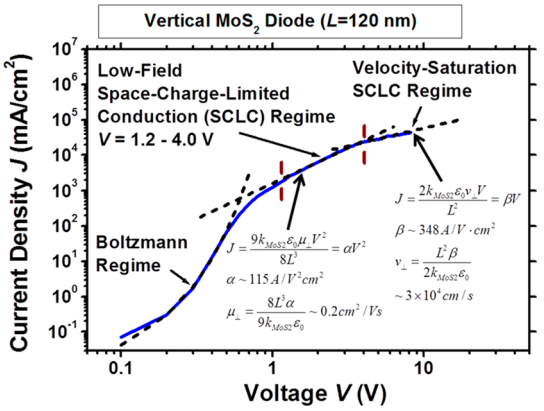

Figure 7. Forward bias $J-V$ characteristic curve, measured without illumination, of a MoS_2 diode consisting of vertically stacked Au/p-doped MoS_2/n-type MoS_2/ITO layers (total MoS_2 thickness ~120 nm), which exhibits different transport characteristics in different bias regimes, including Boltzmann (0−1.2 V), low-field space-charge-limited conduction (SCLC) (1.2−4 V), and velocity-saturation SCLC (>4 V) regimes.

transport characteristics in different bias regimes, including Boltzmann (V = 0−1.2 V), low-field space-charge-limited conduction (SCLC) (V = 1.2−4 V), and velocity-saturation SCLC ($V > 4$ V) regimes. In particular, in the low-field SCLC regime, the $J-V$ curve can be well fitted with eq 1 (*i.e.*, the Mott−Gurney equation for the low-field SCLC regime),[34,35] where k_{MoS2} is the effective dielectric constant of multilayer MoS_2 ($k_{MoS2} \sim 10$);[36,37] ε_0 is the vacuum permittivity; $\mu_\perp$ is the field-effect mobility along the direction perpendicular to MoS_2 layers. Here, the coefficient $\alpha = 9k_{MoS2}\varepsilon_0\mu_\perp/8L^3$ is fitted to be ~115 A/V^{2}cm^2, and $\mu_\perp = 8L^3\alpha/9k_{MoS2}\varepsilon_0$ is estimated to be ~0.2 cm^2/(V s) that is about 2 orders of magnitude lower than typical in-plane mobility ($\mu_{//}$) values of MoS_2 layers.

$$J = \frac{9k_{MoS2}\varepsilon_0\mu_\perp V^2}{8L^3} = \alpha V^2 \quad (1)$$

$$J = \frac{2k_{MoS2}\varepsilon_0 v_\perp V}{L^2} = \beta V \quad (2)$$

In the velocity-saturation SCLC regime, the $J-V$ curve can be fitted with eq 2 (*i.e.*, the Mott−Gurney equation for the velocity-saturation SCLC regime),[34,35] where $v_\perp$ is the saturation velocity along the direction perpendicular to MoS_2 layers. The coefficient $\beta = 2k_{MoS2}\varepsilon_0 v_\perp/L^2$ is fitted to be ~348 A/Vcm^2, and $v_\perp$ is estimated to be ~3 × 10^4 cm/s that is also about 2 orders of magnitude lower than the in-plane saturation velocity in MoS_2 layers.[38] In addition, the critical electric field associated with $v_\perp$ is ~3 × 10^5 V/cm that is estimated from the critical voltage (~4 V) of the transition between low-field and velocity-saturation SCLC regimes.

We currently lack a comprehensive model for fully understanding the MoS_2 thickness-dependent behaviors of critical PV parameters that are shown in Figure 5. Such a model should be based on the plasma doping-modulated

TABLE 1. Comparison of Critical Photovoltaic Response Parameters Achieved in Our Plasma-Doped MoS_2 PV Devices with Those of Other LTMD-Based PV-Related Devices or Structures Previously Reported

structure and LTMD thickness (t_{LTMD})	light source	doping method	type of built-in potentials	J_{sc} (mA/cm^2)	EQE (%)	V_{oc} (V)	FF	PCE (%)
vertically stacked Au/MoS_2/ITO PV cells[18] t_{MoS2} = 110–220 nm	AM1.5G	NA	Au/MoS_2 Schottky barriers	2.52–5.37	30–50 for λ =300–700 nm	0.59	0.48–0.55	0.7–1.8
vertically stacked graphene–MoS_2–metal heterostructures[14] $t_{MoS2} \approx$ 50 nm	458–633 nm	NA	electric field from external gates	NA	20–55 for λ =458–633 nm	~0.16 V under zero gate bias	NA	NA
vertically stacked graphene–WS_2–graphene structures[8] t_{WS2} = 5–50 nm	488, 514, 633 nm	water vapor	electric field from external gates	NA	~30 at λ = 633 nm	~0.15 V under a gate bias of −20 V	NA	NA
lateral MoS_2 phototransistors[42] t_{MoS2} = monolayer	550 nm	NA	external drain and gate biases	NA	1.69 at λ = 550 nm	NA	NA	NA
gated lateral MoS_2 Schottky junctions[19] $t_{MoS2} \approx$ 50 nm	532 nm	NA	asymmetric Au-MoS_2–Pd Schottky junctions	9.7 mA/cm^2 under 532 nm illumination with power density of 100 mW/cm^2[a]	~23 at λ = 532 nm[a]	0.1	0.37[a]	~0.36 at λ = 532 nm[a]
multilayer MoS_2 PV cells[43] t_{MoS2} > 200 nm	white light (0.5 AMI, 60 mW/cm^2)	NA	Cu-MoS_2 Schottky barriers	~1 mA/cm^2 at T ~ 120 K	NA	~0.4 V at T ~120 K, but ~0.03 mV at T ~240 K	NA	<1 at T~120 K
monolayer WSe_2 LEDs[20]	660 nm	dual-gates	electrically tunable pn junctions	NA	internal quantum efficiency ~5%	NA	NA	NA
monolayer WSe_2 photodiode[21]	500–1000 nm	dual-gates	electrically tunable pn junctions	NA	0.2 at λ =522 nm	0.5–0.7 V	NA	NA
monolayer WSe_2 PV devices[22]	halogen lamp light, (1400 W/m^2)	dual-gates	electrically tunable pn junctions	~1.6 mA/cm^2[a]	NA	~0.85 V	~0.5	~0.5
vertically stacked Au/MoS_2/ITO PV devices (this work) t_{MoS2} = 50 nm	**AM1.5G**	**plasma**	**p–n junctions**	**7.43**	**12–55 for λ =300–700 nm**	**0.20**	**0.40**	**0.59**
vertically stacked Au/MoS_2/ITO PV devices (this work) t_{MoS2} = 120 nm	**AM1.5G**	**plasma**	**p–n junctions**	**20.9**	**37–78 for λ =300–700 nm**	**0.28**	**0.47**	**2.8**

[a] Derived or estimated values from the references.

band structure of MoS_2 and needs comprehensive data of diffusion lengths and binding energies of photogenerated e−h pairs, positions/depths of p−n junction depletion regions, electric field-dependent recombination rates of carriers, and light extinction coefficients in plasma-doped multilayer MoS_2. Here, we only provide an initial qualitative explanation. The increase of J_{sc} with increasing the MoS_2 thickness in the range of 10−120 nm could be attributed to the increase of the total absorption of incident light and the total amount of photogenerated carriers. The low J_{sc} values observed in devices with MoS_2 thicknesses >210 nm (Figure S5. Supporting Information) may be due to the limited diffusion lengths of photogenerated carriers that in turn would result in a low collection efficiency of carriers at the electrodes. Although the origins of V_{oc} and FF parameters of MoS_2 PV devices are still not clear, the previous works on c-Si, α-Si, and organic PV cells imply that they are probably associated with multiple factors, including built-in potentials ($\Delta\Phi_{in}$) at p−n junctions, shunt resistance (R_{sh}), series resistance (R_s), generation rate of carriers per unit photoactive area (G), disorder, temperature (T), and the work functions of electrodes.[39−41] Here, R_{sh}, R_s, G values are dependent on the MoS_2 thickness. The increase of MoS_2 thickness in the range of 10−120 nm can enhance the absorption of incident light and the generation rate of carriers (G), which could increase the quasi-Fermi level difference between electrons and holes, and therefore increase V_{oc}. This mechanism is expected to be coupled with an increase of J_{sc}. In addition, the increase of MoS_2 thickness is expected to reduce the current leakage through the tunneling channels and pin-holes in MoS_2 flakes, which could increase R_{sh} and therefore V_{oc} as well as FF values. However, when the MoS_2 thickness is overly thick (*e.g.*, t_{MoS2} > 210 nm), R_s may be too high and degrade the FF value.[39−41]

Finally, we systematically compare the critical photovoltaic response parameters achieved in our plasma-doped MoS_2 PV devices with those of relevant LTMD-based photodevices reported by other groups, which are listed in Table 1.[8,12,14,18,42,43] To the best of our knowledge, under the standard AM1.5G illumination our CHF_3 plasma-doped PV devices with 100−120 nm thick MoS_2 photoactive layers exhibit the highest J_{sc}, EQE, and PCE values among current LTMD-based PV-related devices with similar photoactive layer thicknesses.[18,43] It is noted that our PV devices as well as other recently reported vertically stacked LTMD heterostructure PV devices exhibit relatively low values of V_{oc} (lower than 0.6 V; mostly in the range 0.1−0.3 V). Such low V_{oc} values could be attributed to pinholes or edge leakage defects in current MoS_2 flakes, which may result in undesirable leakage between electrodes, relatively low shunt resistance (R_{sh}), and hence relatively low V_{oc}.[39−41] Such a pinhole or edge-leakage effect is expected to become more serious with reduction of MoS_2 thickness. To support this analysis, we plot R_{sh} values of our CHF_3-doped devices as a function of their MoS_2 photoactive layer thicknesses (Figure S11 (a)) (Supporting Information). Figure S11 (a) (Supporting Information) shows that R_{sh} indeed decreases with reduction of MoS_2 thickness. In addition, the V_{oc} values of our devices also exhibit a strong correlation with R_{sh} values (*i.e.*, V_{oc} decreases with reduction of R_{sh}, as demonstrated in Figure S11 (b), Supporting Information). These experimental data support our conclusion that pinholes or edge leakage defects would be likely responsible for the relatively low V_{oc} values of current vertically stacked LTMD PV devices. With the development of new methods enabling the growth of high-quality MoS_2 films with a lower defect density and the reliable passivation of the edge leakage states of MoS_2 flakes, the V_{oc} values of vertically stacked LTMD PV devices would be significantly improved in the future.

CONCLUSION

In conclusion, this work has provided a solid foundation to prove that the plasma-assisted doping can serve as a reliable approach to form stable p−n junctions in multilayer MoS_2 and result in a significant enhancement of photovoltaic response in MoS_2-based PV devices. We have applied this doping method to make a vertically stacked Au/p-doped MoS_2/n-type MoS_2/ITO PV structure and achieved reasonably good PCE values up to 2.8% and very high J_{sc} values up to 20.9 mA/cm^2 under AM1.5G illumination, as well as high EQE values in the range of 37−78% for wavelengths ranging from 300 to 700 nm. These are the highest values of PCE, J_{sc}, and EQE for LTMD-based PV devices ever reported to date. This work also suggests that the photovoltaic response performance of MoS_2 PV devices highly depends on the MoS_2 photoactive layer thicknesses, and the optimal MoS_2 thickness for achieving the highest performance may be in the range of 120−210 nm. We anticipate that this work could advance new technical approaches for tailoring the band structures of emerging atomically layered 2D materials, and provide critical and imperative scientific insights for leveraging the unique optoelectronic properties of these materials for photovoltaic and other optoelectronic applications.

MATERIALS AND METHODS

Fabrication of PV Devices with Plasma-Doped MoS_2 Photoactive Layers. The bulk MoS_2 ingot samples were purchased from SPI, Inc., with sample size ~1 cm^2. The prepatterning of the MoS_2 ingot stamps was performed by using a previously published method.[17] The top surface layers of MoS_2 ingot stamps were treated (or doped) with various plasmas (*i.e.*, O_2, SF_6, CF_4, and CHF_3) in a standard reactive ion etching (RIE) tool (Plasma-Therm 790 Etcher). For all plasma recipes, the RF power was fixed to 100 W; the pressure was 10 mTorr; the precursor gas flow rate was 10 sccm; and the treatment time was 1 min.

The surface analysis of plasma-doped MoS_2 flakes was performed by using an X-ray photoelectron spectroscope (XPS, Model: Kratos Axis Ultra XPS). To exfoliate the plasma-treated MoS_2 flake pixels onto the device substrates, the MoS_2 ingot stamps were pressed onto the prepatterned Au cathodes on substrates and subsequently released by using a custom-made pressing tool. These Au cathodes (5 nm of Ti/70 nm of Au) were fabricated by photolithography followed by metal deposition and lift-off. To form the anode electrodes, 50 nm ITO films were deposited on top of the exfoliated multilayer MoS_2 flakes by using an ion-beam sputter (Kurt J. Lesker Lab 18-1). The as-deposited ITO films were thermally annealed in a vacuum chamber at 300 °C for 40 min to enhance their conductivity and transparency.

PV and EQE Characterizations. Current density versus voltage ($J-V$) characteristic curves were measured by using a Keithley 2400 system equipped with an Oriel Sol3A solar simulator (AM1.5G, Class AAA, Newport) that was calibrated by using a NREL-certified Si reference cell. The EQE data as a function of wavelengths were measured by using a luminescence spectrometer (AMINCO-Bowman series 2) with a slit width of 16 nm as the light source. The spectral irradiance of this instrument ranges from ~25−200 $\mu W/mm^2$ over the wavelength range from 300 to 800 nm, and it was calibrated using a Newport 818-UV detector. Photocurrents were quantified with a Keithley 6514 electrometer. In addition, to enable a preliminary identification of the optimal plasma recipes for doping MoS_2 PV devices, a 532 nm laser (power density, 283 mW/cm^2) was also employed to quickly characterize the PV response performance of the devices doped with various plasmas.

Conflict of Interest: The authors declare no competing financial interest.

Supporting Information Available: $I-V$ characteristics of MoS_2 PV devices treated with O_2, SF_6, CF_4, and CHF_3 plasma recipes measured under illumination of 532 nm laser light (Figure S1); $J-V$ characteristics of several CHF_3 plasma-treated PV devices (MoS_2 photoactive layer thicknesses: 81−120 nm) fabricated in the same batch (Figure S2); responsivity spectrum and $I-V$ characteristics of a CHF_3 plasma-treated PV device (Figure S3); $J-V$ characteristics, measured under AM1.5G illumination, of all CHF_3 plasma-doped and undoped PV devices with different MoS_2 photoactive layer thicknesses (Figure S4); $J-V$ characteristics, measured under AM1.5G illumination, of several CHF_3 plasma-doped PV devices with MoS_2 photoactive layer thicknesses >200 nm (Figure S5); in-depth discussion of plasma-assisted doping processes; angle-resolved XPS characterization of a CHF_3 plasma-doped MoS_2 flake (Figure S6); XPS surface analysis of CHF_3 plasma-doped and undoped (pristine) MoS_2 flakes at different locations (Figure S7); evaluation of ITO/untreated n-type MoS_2 interfaces (Figure S8); band diagrams of Au/untreated n-type MoS_2 interfaces (Figure S9); additional analysis of Au/plasma-treated MoS_2 interfaces (Figure S10); analysis of open-circuit voltage V_{oc} values of CHF_3 plasma-doped PV devices (Figure S11). This material is available free of charge *via* the Internet at http://pubs.acs.org.

Acknowledgment. This work is supported by NSF Grant No. CMMI-1232883. We thank the staff of the Univeristy of Michigan's North Campus Electron Microbeam Analysis Laboratory for providing support for XPS characterization the staff of the University of Michigan's Lurie Nanofabrication Facility for providing support for AFM imaging and device fabrication.

REFERENCES AND NOTES

1. Radisavljevic, B.; Radenovic, A.; Brivio, J.; Giacometti, V.; Kis, A. Single-Layer MoS_2 Transistors. *Nat. Nanotechnol.* **2011**, *6*, 147–150.
2. Pu, J.; Yomogida, Y.; Liu, K. K.; Li, L. J.; Iwasa, Y.; Takenobu, T. Highly Flexible MoS_2 Thin-Film Transistors with Ion Gel Dielectrics. *Nano Lett.* **2012**, *12*, 4013–4017.
3. Korn, T.; Heydrich, S.; Hirmer, M.; Schmutzler, J.; Schuller, C. Low-Temperature Photocarrier Dynamics in Monolayer MoS_2. *Appl. Phys. Lett.* **2011**, *99*, 102109/1–102109/3.
4. Mak, K. F.; Lee, C.; Hone, J.; Shan, J.; Heinz, T. F. Atomically Thin MoS_2: A New Direct-Gap Semiconductor. *Phys. Rev. Lett.* **2010**, *105*, 136805/1–136805/4.
5. Chhowalla, M.; Shin, H. S.; Eda, G.; Li, L. J.; Loh, K. P.; Zhang, H. The Chemistry of Two-Dimensional Layered Transition Metal Dichalcogenide Nanosheets. *Nat. Chem.* **2013**, *5*, 263–275.
6. Xiao, D.; Liu, G. B.; Feng, W. X.; Xu, X. D.; Yao, W. Coupled Spin and Valley Physics in Monolayers of MoS_2 and Other Group-VI Dichalcogenides. *Phys. Rev. Lett.* **2012**, *108*, 196802/1–196802/5.
7. Tsai, D. S.; Liu, K. K.; Lien, D. H.; Tsai, M. L.; Kang, C. F.; Lin, C. A.; Li, L. J.; He, J. H. Few-Layer MoS_2 with High Broadband Photogain and Fast Optical Switching for Use in Harsh Environments. *ACS Nano* **2013**, *7*, 3905–3911.
8. Britnell, L.; Ribeiro, R. M.; Eckmann, A.; Jalil, R.; Belle, B. D.; Mishchenko, A.; Kim, Y. J.; Gorbachev, R. V.; Georgiou, T.; Morozov, S. V.; et al. Strong Light-Matter Interactions in Heterostructures of Atomically Thin Films. *Science* **2013**, *340*, 1311–1314.
9. Eda, G.; Maier, S. A. Two-Dimensional Crystals: Managing Light for Optoelectronics. *ACS Nano* **2013**, *7*, 5660–5665.
10. Mattheis, Lf Band Structures of Transition-Metal-Dichalcogenide Layer Compounds. *Phys. Rev. B* **1973**, *8*, 3719–3740.
11. Bernardi, M.; Palummo, M.; Grossman, J. C. Extraordinary Sunlight Absorption and One Nanometer Thick Photovoltaics Using Two-Dimensional Monolayer Materials. *Nano Lett.* **2013**, *13*, 3664–3670.
12. Chang, H. Y.; Yang, S. X.; Lee, J. H.; Tao, L.; Hwang, W. S.; Jena, D.; Lu, N. S.; Akinwande, D. High-Performance, Highly Bendable MoS_2 Transistors with High-*k* Dielectrics for Flexible Low-Power Systems. *ACS Nano* **2013**, *7*, 5446–5452.
13. Yu, W. J.; Li, Z.; Zhou, H. L.; Chen, Y.; Wang, Y.; Huang, Y.; Duan, X. F. Vertically Stacked Multi-Heterostructures of Layered Materials for Logic Transistors and Complementary Inverters. *Nat. Mater.* **2013**, *12*, 246–252.
14. Yu, W. J.; Liu, Y.; Zhou, H.; Yin, A.; Li, Z.; Huang, Y.; Duan, X. Highly Efficient Gate-Tunable Photocurrent Generation in Vertical Heterostructures of Layered Materials. *Nat. Nanotechnol.* **2013**, *8*, 952–958.
15. Bae, S.; Kim, H.; Lee, Y.; Xu, X. F.; Park, J. S.; Zheng, Y.; Balakrishnan, J.; Lei, T.; Kim, H. R.; Song, Y. I.; et al. Roll-To-Roll Production of 30-in. Graphene Films for Transparent Electrodes. *Nat. Nanotechnol.* **2010**, *5*, 574–578.
16. Liang, X. G.; Giacometti, V.; Ismach, A.; Harteneck, B. D.; Olynick, D. L.; Cabrini, S. Roller-Style Electrostatic Printing of Prepatterned Few-Layer-Graphenes. *Appl. Phys. Lett.* **2010**, *96*, 013109/1–013109/3.
17. Nam, H.; Wi, S.; Rokni, H.; Chen, M. K.; Priessnitz, G.; Lu, W.; Liang, X. G. MoS_2 Transistors Fabricated *via* Plasma-Assisted Nanoprinting of Few-Layer MoS_2 Flakes into Large-Area Arrays. *ACS Nano* **2013**, *7*, 5870–5881.
18. Shanmugam, M.; Durcan, C. A.; Yu, B. Layered Semiconductor Molybdenum Disulfide Nanomembrane Based Schottky-Barrier Solar Cells. *Nanoscale* **2012**, *4*, 7399–7405.
19. Fontana, M.; Deppe, T.; Boyd, A. K.; Rinzan, M.; Liu, A. Y.; Paranjape, M.; Barbara, P. Electron-Hole Transport and Photovoltaic Effect in Gated MoS_2 Schottky Junctions. *Sci. Rep.* **2013**, *3*, 1634/1–1634/5.
20. Ross, J. S.; Klement, P.; Jones, A. M.; Ghimire, N. J.; Yan, J.; Mandrus, D. G.; Taniguchi, T.; Watanabe, K.; Kitamura, K.; Yao, W.; et al. Electrically Tunable Excitonic Light-Emitting Diodes Based on Monolayer WSe_2 P−N Junctions. *Nat. Nanotechnol.* **2014**, *9*, 268–72.
21. Baugher, B. W.; Churchill, H. O.; Yang, Y.; Jarillo-Herrero, P. Optoelectronic Devices Based on Electrically Tunable P−N Diodes in A Monolayer Dichalcogenide. *Nat. Nanotechnol.* **2014**, *9*, 262–267.
22. Pospischil, A.; Furchi, M. M.; Mueller, T. Solar-Energy Conversion and Light Emission in an Atomic Monolayer P−N Diode. *Nat. Nanotechnol.* **2014**, *9*, 257–261.
23. Chen, M.; Nam, H.; Wi, S.; Lian, J.; Ren, X.; Bian, L. F.; Lu, S.; Liang, X. G. Stable Few-Layer MoS_2 Diodes Formed by

Plasma-Assisted Doping. *Appl. Phys. Lett.* **2013**, *103*, 142110/1–142110/4.
24. Green, M. A.; Emery, K.; Hishikawa, Y.; Warta, W.; Dunlop, E. D. Solar Cell Efficiency Tables (Version 43). *Prog. Photovoltaics* **2014**, *22*, 1–9.
25. Liang, D.; Kang, Y. S.; Huo, Y. J.; Chen, Y. S.; Cui, Y.; Harris, J. S. High-Efficiency Nanostructured Window GaAs Solar Cells. *Nano Lett.* **2013**, *13*, 4850–4856.
26. Wang, T. H.; Iwaniczko, E.; Page, M. R.; Levi, D. H.; Yan, Y.; Yelundur, V.; Branz, H. M.; Rohatgi, A.; Wang, Q. Effective Interfaces in Silicon Heterojunction Solar Cells. *Conf. Rec. 31st IEEE Photovoltaic Spec. Conf.* **2005**, 955–958.
27. Ward, J. S.; Ramanathan, K.; Hasoon, F. S.; Coutts, T. J.; Keane, J.; Contreras, M. A.; Moriarty, T.; Noufi, R. A 21.5% Efficient Cu(In,Ga)Se-2 Thin-Film Concentrator Solar Cell. *Prog. Photovoltaics* **2002**, *10*, 41–46.
28. Wu, X. Z. High-Efficiency Polycrystalline CdTe Thin-Film Solar Cells. *Sol. Energy* **2004**, *77*, 803–814.
29. Ferekides, C.; Britt, J. Cdte Solar Cells with Efficiencies over 15%. *7th Int. Photovoltaic Sci. Eng. Conf., Technical Digest* **1993**, 509–511.
30. Caballero, A.; Espinos, J. P.; Fernandez, A.; Soriano, L.; Gonzalez Elipe, A. R. Adsorption and Oxidation of K Deposited on Graphite. *Surf. Sci.* **1996**, *364*, 253–265.
31. Fang, H.; Tosun, M.; Seol, G.; Chang, T. C.; Takei, K.; Guo, J.; Javey, A. Degenerate n-Doping of Few-Layer Transition Metal Dichalcogenides by Potassium. *Nano Lett.* **2013**, *13*, 1991–1995.
32. Mahns, B.; Roth, F.; Knupfer, M. Absence of Photoemission from The Fermi Level in Potassium Intercalated Picene and Coronene Films: Structure, Polaron, or Correlation physics? *J. Chem. Phys.* **2012**, *136*, 134503/1–134503/6.
33. Park, Y.; Choong, V.; Gao, Y.; Hsieh, B. R.; Tang, C. W. Work Function of Indium Tin Oxide Transparent Conductor Measured by Photoelectron Spectroscopy. *Appl. Phys. Lett.* **1996**, *68*, 2699–2701.
34. Rose, A. Space-Charge-Limited Currents in Solids. *Phys. Rev.* **1955**, *97*, 1538–1544.
35. Sinharay, N.; Meltzer, B. Characteristics of Insulator Diodes Determined by Space-Charge and Diffusion. *Solid-State Electron.* **1964**, *7*, 125–136.
36. Berkelbach, T. C.; Hybertsen, M. S.; Reichman, D. R. Theory of Neutral and Charged Excitons in Monolayer Transition Metal Dichalcogenides. *Phys. Rev. B* **2013**, *88*, 045318/1–045318/6.
37. Cheiwchanchamnangij, T.; Lambrecht, W. R. L. Quasiparticle Band Structure Calculation of Monolayer, Bilayer, and Bulk MoS_2. *Phys. Rev. B* **2012**, *85*, 205302/1–205302/4.
38. Fiori, G.; Szafranek, B. N.; Iannaccone, G.; Neumaier, D. Velocity Saturation in Few-Layer MoS_2 Transistor. *Appl. Phys. Lett.* **2013**, *103*, 233509/1–233509/4.
39. Qi, B. Y.; Wang, J. Z. Open-Circuit Voltage in Organic Solar Cells. *J. Mater. Chem.* **2012**, *22*, 24315–24325.
40. Li, H.; Zhang, Z. G.; Li, Y. F.; Wang, J. Z. Tunable Open-Circuit Voltage in Ternary Organic Solar Cells. *Appl. Phys. Lett.* **2012**, *101*, 163302/1–163302/5.
41. Chou, C. T.; Lin, C. H.; Wu, M. H.; Cheng, T. W.; Lee, J. H.; Liu, C. H. J.; Tai, Y. A.; Chattopadhyay, S.; Wang, J. K.; Chen, K. H.; et al. Tuning Open-Circuit Voltage in Organic Solar Cells by Magnesium Modified Alq(3). *J. Appl. Phys.* **2011**, *110*, 083104/1–083104/5.
42. Yin, Z. Y.; Li, H.; Li, H.; Jiang, L.; Shi, Y. M.; Sun, Y. H.; Lu, G.; Zhang, Q.; Chen, X. D.; Zhang, H. Single-Layer MoS_2 Phototransistors. *ACS Nano* **2012**, *6*, 74–80.
43. Fortin, E.; Sears, W. M. Photo-Voltaic Effect and Optical-Absorption in MoS_2. *J. Phys. Chem. Solids* **1982**, *43*, 881–884.